Evaluation of fracture properties by coupling digital image correlation and Finite Fracture Mechanics

Int J Fract (2025) 249:66
https://doi.org/10.1007/s10704-025-00885-9

RESEARCH

Evaluation of fracture properties by coupling digital image correlation and Finite Fracture Mechanics

Francesco Ferrian · Alberto Sapora · Rafael Estevez · Aurélien Doitrand

Received: 18 January 2025 / Revised: 10 August 2025 / Accepted: 12 August 2025 / Published online: 3 September 2025

Abstract Crack initiation in flattened disks under compression containing either a central or eccentric circular hole is investigated through the Finite Fracture Mechanics (FFM) approach. An implementation of the FFM criterion based on digital image correlation (DIC) full-field measurement is proposed. The coupling between FFM and DIC is provided through boundary conditions taken from the measured displacement fields. This approach offers a more accurate representation of the actual loading conditions compared to the use of idealized prescribed force or displacement in standard FFM implementations. Furthermore, by exploiting the value of the critical energy release rate obtained from the stable crack growth phase analysis, this method enables precise estimations of the inherent material strength and critical crack advance.

Keywords FFM · DIC · Size effect · Energy balance · Elastic properties · Fracture parameters

List of symbols

e	Eccentricity of the hole
R	External radius of the disk
t	Thickness of the sample
α	Loading angle
ρ	Hole radius
E	Young's modulus
υ	Poisson's ratio
ℓ_c	Initiation crack length
ℓ_{ch}	Irwin's length
ℓ_{exp}	Experimental crack length
G_{inc}	Incremental energy release rate
G_{Ic}	Critical value of the energy release rate
K_{Ic}	Fracture toughness
P_c	Experimental initiation load
$P_{c,avg}$	Average value of the experimental initiation loads
U_c	Critical applied displacement
σ_{UTS}	Ultimate tensile strength
σ_0	Inherent strength of the material
σ_{xx}	Normal stress field
(x, y)	Cartesian coordinate system
DIC	Digital image correlation
FFM	Finite fracture mechanics
FEA	Finite element analyses
PMMA	Polymethyl methacrylate
SIF	Stress intensity factor

F. Ferrian (✉) · A. Sapora
Department of Structural, Geotechnical and Building Engineering, Politecnico di Torino, Turin, Italy
e-mail: francesco.ferrian@polito.it

R. Estevez
Université Grenoble-Alpes - CNRS UMR 5266, SIMaP, 38000 Grenoble, France

A. Doitrand
INSA-Lyon, Universite Claude Bernard Lyon 1, CNRS, MATEIS, UMR5510, 69621 Villeurbanne, France

TCD Theory of critical distances

1 Introduction

The strength of structures and mechanical components can be significantly affected by the presence of stress concentrators such as notches or holes. Acting as stress raisers, they result in localized stress concentrations, thereby reducing the load span necessary for maintaining mechanical integrity. Different approaches have been proposed to address the decrease in the load-bearing capacity of structures caused by such stress raisers. Neuber (1936) proposed an approach based on the calculation of an effective stress by averaging the linear elastic stress field ahead of the notch tip over a material characteristic length. Neuber argued that the effective stress should be evaluated within a structural finite volume rather than an infinitesimal volume, as assumed by classical theories. A few years later, Peterson (1938) simplified Neuber's approach by observing that the reference stress could be calculated at a specified distance from the notch tip. Later, Whitney and Nuismer (1974) and Tanaka (1983), proposed combining ultimate tensile strength and fracture toughness to assess the material characteristic length for predicting brittle failure in notched components. Subsequently, Taylor (2007) formalized these stress-based methodologies under the name of the theory of critical distances (TCD). The simplest form of the TCD is the Point Method, which requires that for fracture to occur, the stress must equal the inherent strength of the material σ_0 at a finite distance $L/2$ along the critical crack path. According to the TCD approach, the characteristic material length L depends on the squared ratio between the fracture toughness K_{Ic} and σ_0. On the other hand, different researchers (Awerbuch and Madhukar 1985; Pipes et al. 1979; Tan 1987) demonstrated a dependence of the critical distance on other parameters, such as geometry features. To overcome this issue, the Finite Fracture Mechanics (FFM) criterion was introduced by coupling a stress condition and an energy balance (Leguillon 2002; Cornetti et al. 2006; Weißgraeber et al. 2016b). Unlike TCD, the FFM approach enables determining an initiation crack length, which is not solely a material property but also dependent on both loading conditions and geometry under investigation. FFM was implemented to assess strength predictions for a wide range of structural configurations subjected to different loading conditions. Focusing on the failure behavior of circular holes under biaxial loading, Torabi et al. (2017) investigated the strength of Polymethyl Methacrylate (PMMA) Brazilian disk samples with a central circular hole. Sapora and Cornetti (2018) analyzed different biaxiality ratios considering remote loading configurations. Furthermore, Chao Correas et al. (2023) conducted a comprehensive study on crack initiation from circular holes under biaxial loading by showing agreement among FFM, Cohesive Zone Model, and Phase Field estimations. More recently, the FFM approach was implanted to investigate also more complex structures such as composite laminate. Specifically, Vereecke et al. (2024) conducted experimental tests on a composite laminate with unidirectional carbon fibers and an epoxy matrix. The FFM approach was then implemented to investigate crack onset, proving to be a suitable tool for representing the brittle cracking process. Aranda and Leguillon (2023) implemented the FFM criterion to study the sequential damage mechanism in samples made of a unidirectional thin layer reinforced with long carbon fibers, embedded between two layers reinforced with glass fibers. The FFM approach successfully described the competition between different fracture mechanisms, and theoretical predictions showed good agreement with experimental results. Furthermore, other FFM applications include, for example, the study of thermal shock cracking in alumina–zirconia multi-layer ceramics (Papšík et al. 2024), crack onset and cavitation in hyperelastic adhesives bondings (Rheinschmidt et al. 2024) and hydraulic crack onset in anisotropic rocks (Sakha et al. 2023).

In order to provide accurate strength estimations, both TCD and FFM approaches require the knowledge of K_{Ic} and σ_0. Regarding the value of the fracture toughness, it can be experimentally determined following established standards for polymers (ASTM D5045 2022; ISO13586 2000). These procedures involve testing Compact Tension or Three Point Bending samples at a constant rate until failure occurs. Initially, a sharp notch has to be machined and then a natural crack, with a precise shape and length, needs to be carefully generated at the notch tip. If this is not possible, either due to the sample fracturing during

tapping (as observed in some brittle materials) or the crack being not visible (as seen in some tough materials), then the pre-crack can be machined using a fresh razor blade in a single motion or with a sawing motion. These standard procedures are thus usually very complex and highly time-consuming to perform (Schindler 2018). Alternatively, the value of K_{Ic} can be derived from the Izod absorbed energy measured through Izod impact tests, which are less demanding in terms of time and costs (ASTM D256 2018, ISO 180 2023). However, the main drawback of this procedure is that it offers an indirect measure of fracture toughness based on the energy absorbed during the test, rather than a direct measurement. This absorbed energy is influenced by various factors, including sample configuration, shape of the notch, temperature, strain rate, and loading conditions. Consequently, the Izod test results may not accurately reflect the material's actual fracture behavior (Moore et al. 2001).

An accurate estimate of the fracture toughness can be obtained by monitoring crack propagation and using DIC-based full-field measurements. DIC (Peters and Ranson 1982; Sutton et al. 1983; Pan et al. 2009) is a practical and effective tool for full-field deformation measurement, which has been widely accepted and commonly implemented within experimental mechanics for the determination of material properties and fracture parameters. Indeed, measuring the displacements in the region surrounding the crack tip makes it possible to determine fracture parameters such as cohesive properties, J-integral and Stress Intensity Factor (SIF). In this framework, Shen and Paulino (2011) proposed a hybrid inverse method based on the combined use of DIC and Finite Element Analyses (FEA) to compute the cohesive properties of a ductile adhesive and a quasi-brittle plastic. In this study, they performed tests on single edge-notched beam samples under four-point bending in order to derive the mode I traction–separation relationship. Réthoré and Estevez (2013) performed a micron-scale analysis on PMMA samples to capture and investigate the crazing failure mechanism. During the tests, they used DIC to determine the mode I and II SIFs and the crack tip displacement fields. Furthermore, the onset and growth of the process zone were monitored up to crack onset by using the variation of the equivalent crack tip location. These experimental measurements were then used to accurately define the traction–separation profile of a cohesive zone model. Focusing on the determination of the stress intensity factor value, McNeill et al. (1987) presented a DIC method to determine the SIF in pre-cracked C-specimens and three-point bending samples. Roux and Hild (2006) performed SIF measurements from DIC considering Sandwiched-Beam tests. In this study, they inserted a notched SiC sample between two steel bars and determined the SIF value based on displacements measured through DIC. Hamam et al. (2007) proposed a methodology to determine through DIC techniques the SIF value in Center-Cracked Tension (CTT) specimens made of steel under fatigue loading. The change in the SIF during one fatigue cycle was measured by decomposing the displacement field into a set of elastic fields. More recently, Doitrand et al. (2020) conducted tensile tests on PMMA plates with a central square hole, which resulted in mixed-mode crack onset at the corners of the square hole. The mode I and II generalized SIFs at the V-notches were determined through a path-independent integral, using displacement and strain fields measured directly by DIC. Brittle fracture in sharp V-notched samples was investigated also by Yue et al. (2022). Specifically, the generalized notch SIF and fracture parameters of V-notched rock samples under dynamic impact were measured using DIC techniques. Regarding crack onset and propagation in flattened Brazilian disks, Yan et al. (2021) evaluated the mode I SIF performing experimental tests on sandstone samples and measuring strains and displacements through DIC methods.

As concerns the value of the inherent strength σ_0, it can be considered equal to the ultimate tensile strength σ_{UTS} for brittle and quasi-brittle materials such as ceramics (Taylor 2004) and laminated composites (Whitney and Nuismer 1974). However, if plastic deformation occurs before the final failure, the inherent strength could differ from the value of σ_{UTS} (Susmel and Taylor 2008). Specifically for polymers, due to the presence of defects or micro-cracks and crazing phenomena, the ratio σ_0/σ_{UTS} typically ranges between 1 and 2 (Taylor et al. 2004; Taylor et al. 2005; Sapora et al. 2018). When the inherent strength differs from the ultimate tensile strength, σ_0 can be determined by testing samples of the same material containing sharp and blunt notches, characterized by different stress distributions in the process zone. Indeed, according to the Point Method, the linear-elastic stress field curves at incipient failure should

intersect at the same point for all the different notches. The inherent strength can thus directly be estimated by considering the stress value at this intersection point (Taylor et al. 2004, 2005).

In the framework of FFM, Duminy et al. (2024) proposed a method to determine fracture parameters from DIC performing wedge splitting tests on millimeter-size PMMA specimens. Identification of fracture parameters using the FFM approach usually exploits idealized prescribed force or displacement as boundary conditions. Instead, in this study, Duminy et al. (2024) determined boundary conditions performing full-field measurements during the tests, thus better representing loading conditions on a submodel surrounding the initiation crack location. The FFM approach was used for the inverse identification of fracture properties also by Girard et al. (2023) and Girard et al. (2024). Specifically, in these studies, the fiber-matrix debonding in a single fiber was investigated numerically and experimentally. Then, interface fracture properties were determined to obtain crack initiation/propagation stresses and propagation/debonding arrest angles consistent with experimental observation.

In the present study, a finite element implementation of the FFM approach is presented to investigate crack initiation on disk samples weakened by the presence of either a central or eccentric circular hole. Firstly, elastic material properties are determined by considering the displacement fields measured by DIC and performing 2D linear elastic FEA. To validate the proposed procedure, the obtained values are compared with those derived by following the (ASTM D638 2014) standard code. Then, the FFM criterion is implemented considering a circular submodel and boundary conditions based on displacements measured using DIC. Following this approach, the inherent material strength and critical crack advance are thus precisely estimated using the value of the critical energy release rate obtained from the analysis of the stable crack growth phase.

The structure of the paper is organized as follows: Sect. 2 presents the experimental campaign with the obtained initiation loads. In Sect. 3, the DIC technique is introduced, presenting the methodology implemented to solve the minimization problem. Section 4 outlines the FFM formulation for the geometries investigated in this study. Then, the finite element implementation of the FFM criterion, using boundary conditions derived from DIC-measured displacements, is detailed in Sect. 5. Finally, conclusions are drawn in Sect. 6.

2 Experimental results

Compression tests were performed at a constant displacement rate of 1 mm/min, under uniaxial loading conditions, on disk-shaped samples made of PMMA (depicted in Fig. 1) by Ferrian et al. (2024). The thickness of the samples, denoted as t, was set at 8 mm to ensure plane strain conditions, satisfying the condition $t \geq 2.5\ \ell_{ch}$ (Taylor 2007). Here, $\ell_{ch} = (K_{Ic}/\sigma_0)^2$, representing Irwin's length, typically falls within the range of 0.2–1 mm for PMMA (Taylor 2007; Seweryn 1994).

Two configurations were tested, featuring a central circular hole or an eccentric one with $e = 20$ mm eccentricity. Four hole radii $\rho = 0.5$, 1, 2 and 4 mm were considered for each configuration. For all samples, the outer radius R of the disk is set to 40 mm. Furthermore, the lower and upper regions of the disk were slightly flattened to facilitate sample positioning within the testing machine, as depicted in Fig. 1. This solution, is a common practice aimed at ensuring test effectiveness and enhancing the accuracy of tensile strength estimation. Indeed, this loading configuration ensures crack initiation at the disk

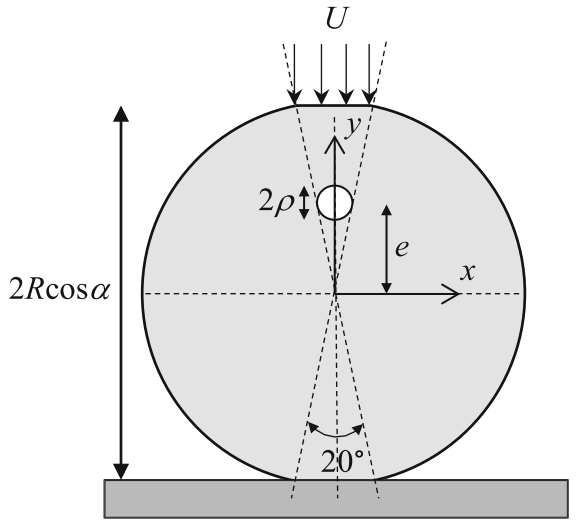

Fig. 1 Sample configuration investigated in the current study presenting a hole with radius ρ and eccentricity e

center, averting localized cracking near the contact zone. The flattened Brazilian Disk (BD) test was introduced by Wang and Xing (1999), and subsequent investigations on the influence of loading angles were conducted by Wang et al. (2004) and Lin et al. (2016). The loading angle was maintained at 20°, consistently with typical experimental practices (Wang and Xing 1999; Wang et al 2004, 2011; Weißgraeber et al. 2016a, b; Whitney and Nuismer 1974; Wu et al. 2018).

Five specimens were considered for each value of hole radius and eccentricity. Although some samples experienced failure within the contact zone, at least three initiation load values P_c were recorded for each geometry. The initiation loads obtained for 32 samples are reported in Table 1.

Notably, the presence of an eccentric hole resulted in decreased strength compared to geometries featuring a central hole. Specifically, for radii values of 0.5 mm and 4 mm, P_c values related to the geometries with a central hole were 10% higher than those registered for e = 20 mm. This discrepancy diminishes to approximately 2% for ρ = 1 mm and 2 mm.

Finally, it is important to highlight that stable crack growth was observed for all the samples before the final failure, except for ρ = 4 mm, e = 0, 20 mm and ρ = 2 mm, e = 0 mm. When stable crack propagation was detected, failure loads were approximately 2–3% higher than the initiation ones.

3 Digital image correlation

DIC stands out as an effective non-contact optical technique for full-field displacement and strain measurement. It works by capturing sequential images of the same object and extracting the displacement fields to attain the most accurate match in the Region of Interest (ROI) between the reference image and the deformed ones (Hild and Roux 2012; Pan 2011). This can be accomplished by employing several criteria and optimization algorithms.

In this study, an algorithm is utilized to minimize the sum of the squared grey level differences between the reference image and the deformed one, adjusted by the displacement field estimation U_e. Denoting with f and g be the grey level fields of reference and deformed images, respectively, and with U the sought displacement field, the following expression is derived (Hild et al. 2015):

$$U = \underset{U_e}{\text{Argmin}} \sum_{\text{ROI}} [f(x) - g(x + U_e(x))]^2 \quad (1)$$

This minimization problem is solved by exploiting the software Ufreckles (Rethoré 2018) which implements a FE-based nonlinear least-squares algorithm.

During the test campaign performed by (Ferrian et al. 2024), images were acquired exploiting a Prosilica GX 6600 camera, with a 2392 (H) × 2774 (V) pixel resolution and considering an acquisition rate of 1 fps. DIC measurements are inherently influenced by acquisition noise related especially to the quality of the speckles, DIC mesh size, lighting and acquisition equipment setup. In order to minimize the noise influence, samples were carefully prepared coating the surface with white and black sprays to obtain high-quality speckles. Furthermore, an unstructured mesh with 3-node triangular elements is adopted setting the mesh size equal to 60 pixels, corresponding to ≈ 1.25 mm. In this way, a good balance between surface partitioning and measurement noise is obtained. A rigid body motion of the disk is analyzed through DIC to estimate the displacement

Table 1 Recorded initiation loads P_c and standard deviations for each tested sample

e (mm)	ρ (mm)	P_c (N)					$P_{c,\,avg}$ (N)
Sample n°		1	2	3	4	5	
0	0.5	15,303	15,077	14,984	–	–	15,122 ± 134
	1	12,642	10,779	11,420	–	–	11,614 ± 773
	2	12,238	11,888	9014	9070	–	10,553 ± 1516
	4	9919	10,650	10,404	11,906	–	10,720 ± 734
20	0.5	13,244	14,113	13,974	13,553	13,081	13,593 ± 400
	1	12,532	10,620	10,071	12,556	–	11,445 ± 1117
	2	11,220	12,886	9270	7701	10,381	10,292 ± 1752
	4	9873	9753	9668	9868	–	9791 ± 85

measurement uncertainty. By computing the standard deviation of the displacements, a measurement uncertainty of ± 0.0011 mm and ± 0.0015 mm is determined for U_x and U_y, respectively.

Figure 2a, b illustrate the displacements along the x-axis and y-axis, respectively, for a disk sample with e = 0 mm and ρ = 4 mm. For the same sample, the x-, y-, and xy-components of the strain field are depicted in Fig. 3. To reduce the measurement noise, the ROI contour shape is defined inside the sample, sufficiently far from the contact zones and the hole edge.

4 Finite fracture mechanics

Considering the geometries with a central circular hole, asymmetric crack initiation from the hole edge along the y-axis is investigated. Theoretically, a symmetric crack initiation should be preferred since it is more critical from an energetic standpoint (Sapora et al. 2018). However, experimentally, an asymmetric crack initiation is observed for all the tested samples. Additionally, theoretical predictions provided by FFM for symmetric and asymmetric crack initiation are very close, with differences lower than 1% (Ferrian et al. 2024).

Analogously, when considering the geometries with e = 20 mm, crack initiation is evaluated according to the FFM approach, considering asymmetric crack initiation from the top of the hole edge. Indeed, this scenario results to be the most critical one, as presented by Ferrian et al. (2024).

According to the FFM approach proposed by Leguillon (2002), finite crack initiation occurs when stress and energy conditions are simultaneously satisfied. The stress requirement imposes that the normal stress σ_{xx} must exceed the material inherent strength σ_0 over a finite distance ℓ. Alternatively, the approach can be implemented considering an average stress condition (Cornetti et al. 2006), resulting in the following expression:

$$\overline{\sigma}_{xx}(\ell) = \frac{1}{\ell}\int_0^{\ell} \sigma_{xx}(y)\mathrm{d}y \geq \sigma_0. \tag{2}$$

Conversely, the energy balance ensures that the Incremental Energy Release Rate (IERR) G_{inc} is larger than the critical ERR value G_{Ic}:

$$G_{inc}(\ell) = -\frac{\Delta W_{el}(\ell)}{\ell} \geq G_{Ic}, \tag{3}$$

where ΔW_{el} is the elastic strain energy variation due to finite crack advance ℓ. It is worth noting that this expression is valid for a displacement-controlled test (ΔW_{ext} = 0) and considering quasi-static loading

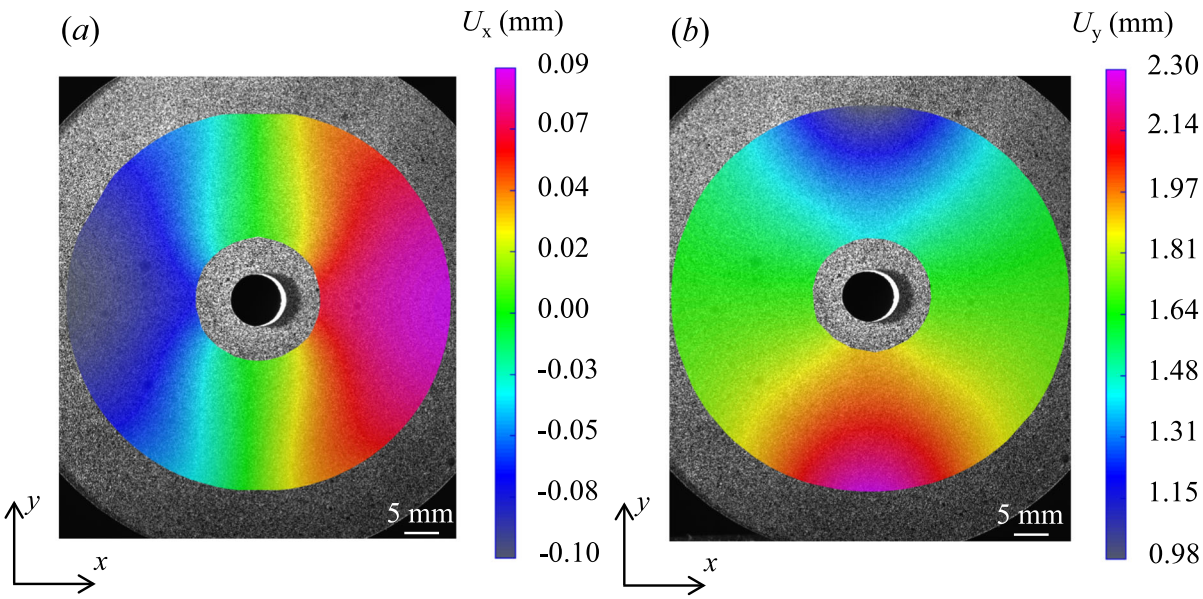

Fig. 2 **a** Horizontal and **b** vertical displacements measured by DIC, immediately before crack initiation, for a sample with e = 0 mm and ρ = 4 mm

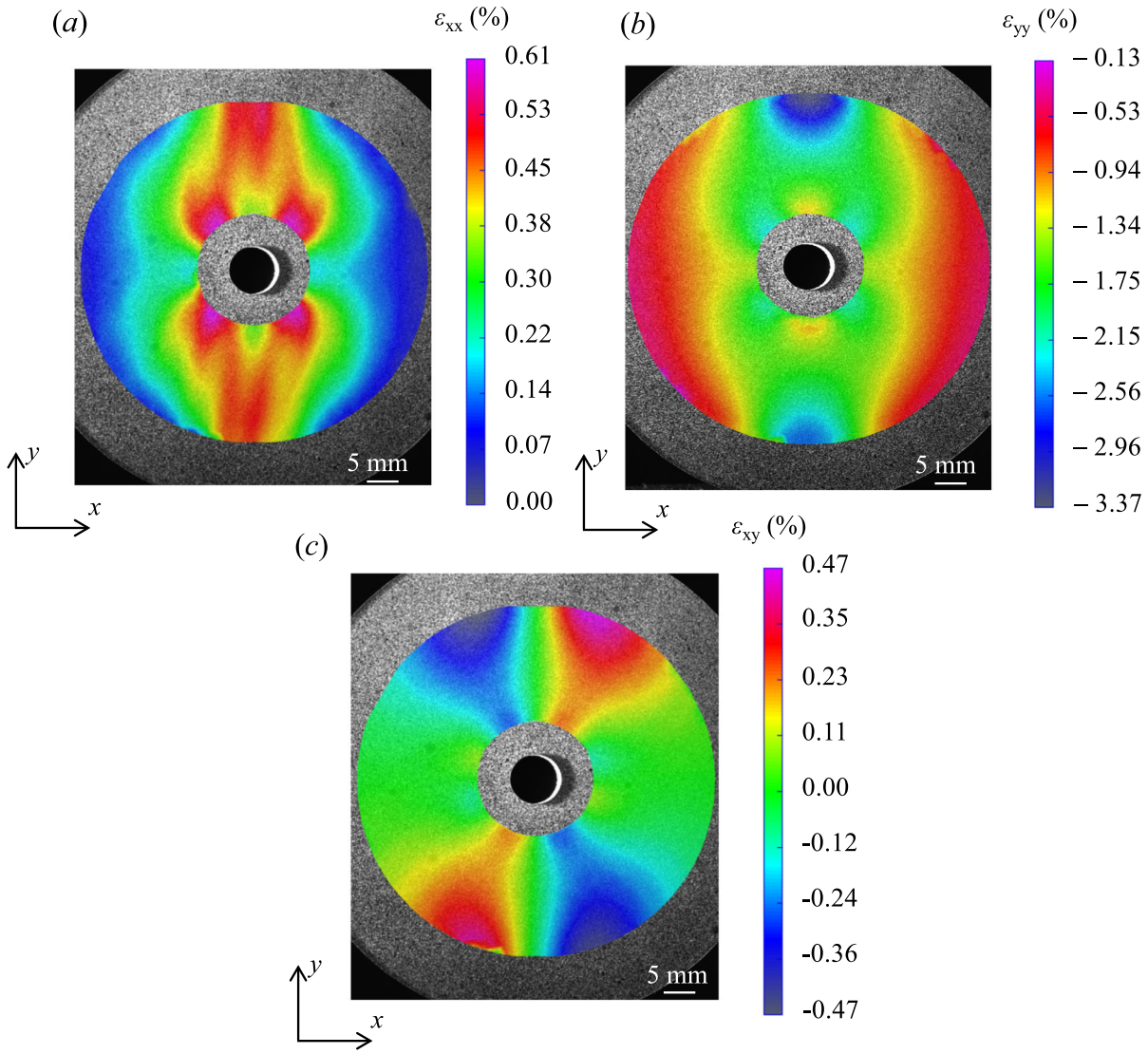

Fig. 3 Strain field components obtained by DIC, immediately before crack initiation, for a sample with e = 0 mm and ρ = 4 mm

conditions ($\Delta W_k \geq 0$). Moreover, Eq. (3) does not account for the energy dissipated by non-linear mechanisms.

Following the formalism presented by Weißgraeber et al. (2016a), the energy release rate function can either increase (positive geometry) or decrease (negative geometry) as the crack propagates. This behavior is influenced by various factors, including material anisotropy, specimen geometry and loading conditions (Felger et al. 2017; Sakha et al. 2023).

Coupling Eqs. (2) and (3), and considering a monotonically increasing IERR function (positive geometry), the following system is obtained:

$$\begin{cases} \overline{\sigma}_{xx}(\ell_c, U_c) = \sigma_0, \\ G_{inc}(\ell_c, U_c) = G_{Ic}, \end{cases} \tag{4}$$

where ℓ_c is the finite crack advance and U_c the critical applied displacement.

System (4) holds also for an initially positive, globally negative geometry (Mantič 2009; Weißgraeber et al. 2016a) if $\ell_c < \ell^*$, where ℓ^* denotes the crack length maximizing G_{inc}. Instead, if the solution of the system yields $\ell_c > \ell^*$, the FFM criterion is expressed by imposing $\ell = \ell^*$ in the energy balance (4) (Mantič 2009).

5 FFM DIC-based implementation

5.1 Determination of submodel size

To perform the DIC-based implementation of the FFM criterion, a circular submodel concentric with the hole is considered (Fig. 4a). The analysis is conducted using a 2D FE model, thus assuming a straight crack front shape. As reported in Ferrian et al. (2024), the actual crack front in the tested samples is not perfectly straight. However, this assumption enabled us to capture the phenomenon with a substantial reduction in computational time compared to implementing a 3D FE model with the measured crack front shape for each sample.

To ensure accurate computation of crack initiation, it is essential to first determine the appropriate submodel size in order to correctly compute $\overline{\sigma}_{xx}(\ell)$ and $G_{inc}(\ell)$ functions. For this purpose, considering configurations with a central hole, a FE model of the full geometry is developed for each radius value, with an applied displacement $U = 1$ mm (Fig. 4a). Then, the average stress field and IERR functions are obtained exploiting the "unbuttoning" method through Eqs. (2) and (3). A mesh with 4-node bilinear plane strain elements is adopted with a minimum

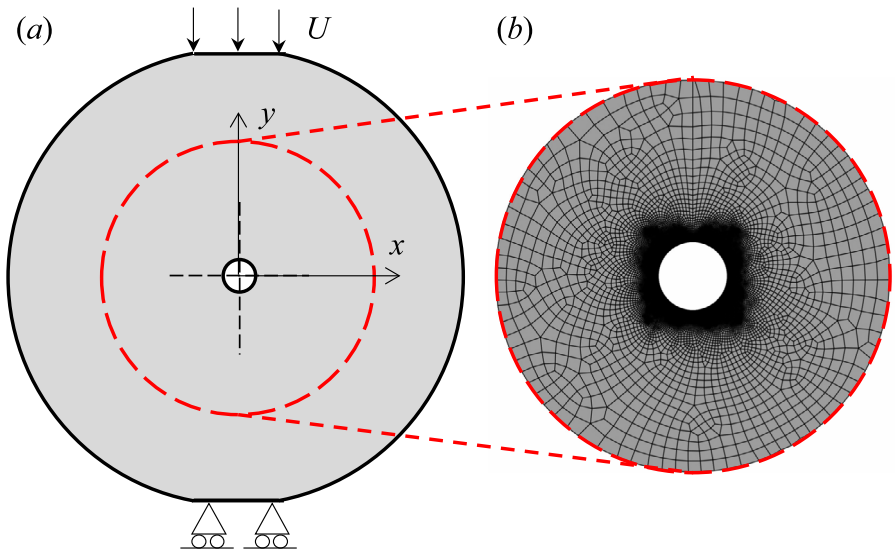

Fig. 4 **a** Schematization of FE model implemented to determine the submodel size and **b** detail of FE mesh characterizing the submodel

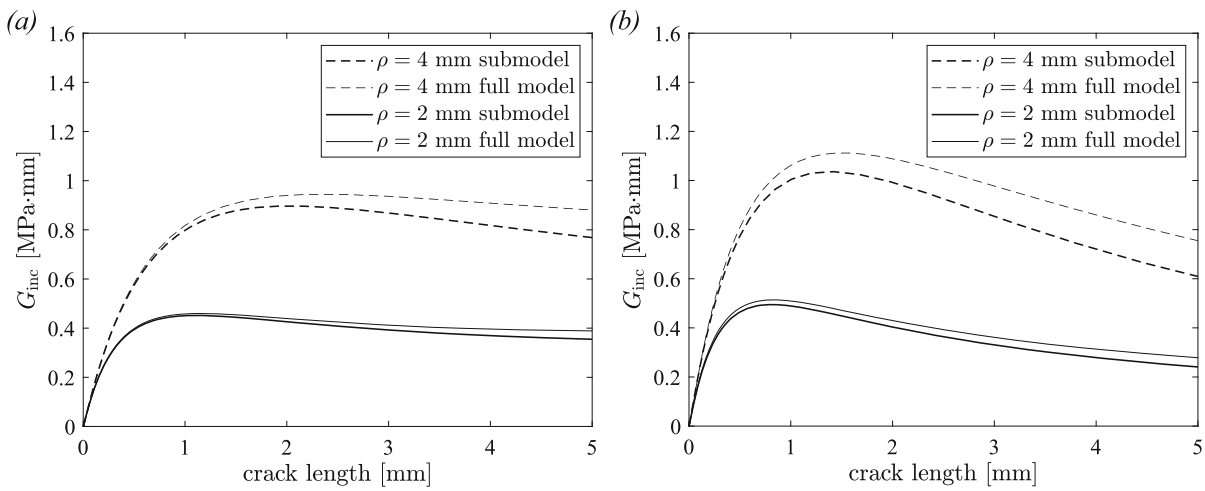

Fig. 5 Comparison between IERR functions obtained by FEA on full model and submodel related to configurations with a **a** central and **b** eccentric hole

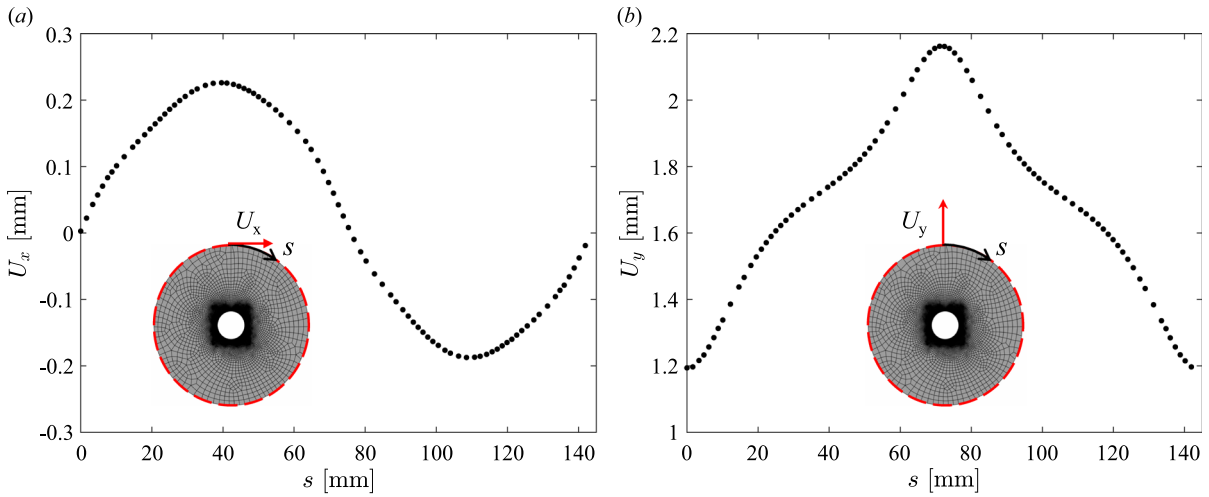

Fig. 6 Displacements **a** U_x and **b** U_y measured by DIC just before crack initiation and imposed as boundary conditions to the contour of the circular FE model. Displacements are reported as a function of the curvilinear abscissae s

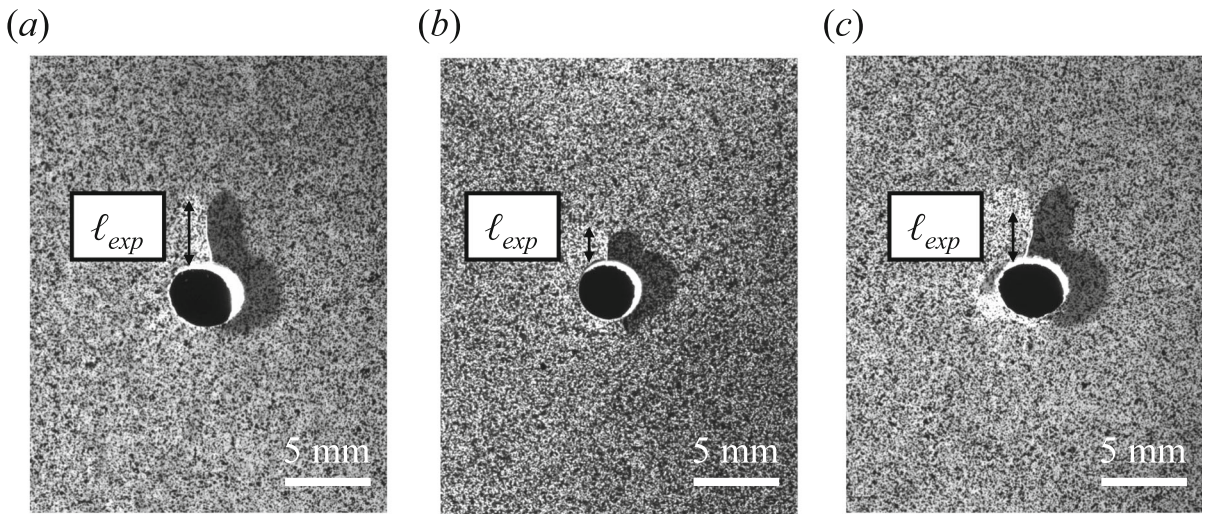

Fig. 7 Images of three different samples with $\rho = 2$ mm and $e = 20$ mm with the detail of the crack length ℓ_{exp} measured experimentally

element size equal to 0.05 mm, following a convergence analysis. Analogously, the functions related to a submodel with a radius of 23 mm (corresponding to approximately 900 pixels) are derived by applying the displacement values determined from the FE full model as boundary conditions (Fig. 4b).

The average stress functions obtained by FEA on the submodel are identical to those computed from the full model, for all radii values. Instead, differences are higher when considering the IERR functions, especially as the crack length ℓ increases. In particular, for $\rho = 2$ mm and 4 mm, the discrepancy is lower than 1% for $\ell < 0.5$ mm and $\ell < 0.4$ mm, respectively. The comparison for these radii values is depicted in Fig. 5a. Considering a higher value of the initiation length $\ell = 3$ mm, the deviation is slightly lower than 5% for $\rho = 2$ mm and around 7% for $\rho = 4$ mm, respectively.

The same analysis is developed on the geometries with an eccentric hole. Due to the proximity of the hole

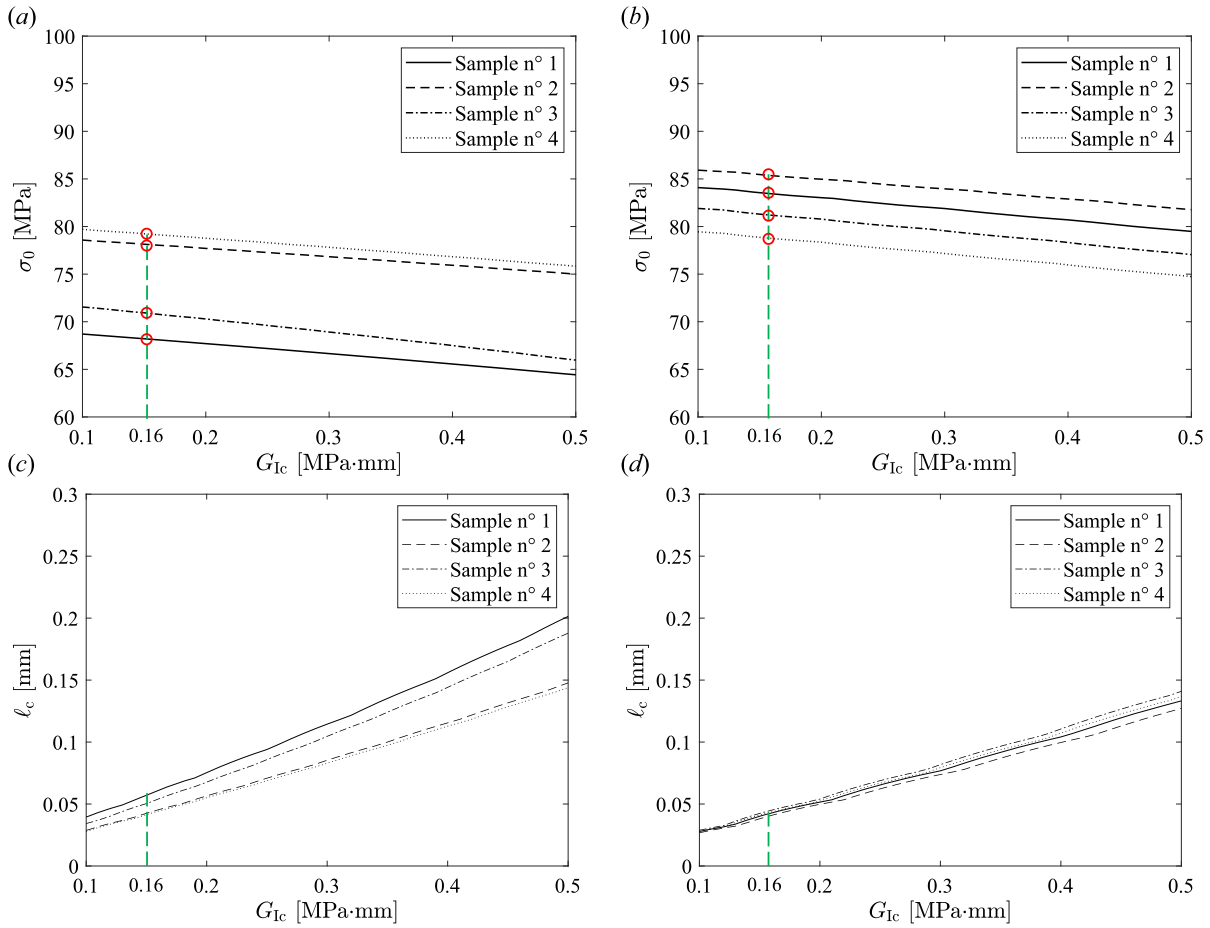

Fig. 8 Couples of values σ_0 and G_{Ic} satisfying FFM system (4) for the four tested samples with $\rho = 4$ mm, **a** $e = 0$ mm and **b** $e = 20$ mm. Additionally, critical crack advance values for each (σ_0, G_{Ic}) pair are depicted in **c** and **d** for $e = 0$ mm and $e = 20$ mm, respectively

to the contact zone, the submodel size for these configurations is smaller, set at 18 mm (approximately 700 pixels). The comparison between IERR functions for $\rho = 2$ mm and 4 mm is depicted in Fig. 5b. In this case discrepancies are higher due to the smaller submodel size, lower than 1% considering $\ell < 0.3$ mm and $\ell < 0.2$ mm for $\rho = 2$ mm and 4 mm, respectively. Taking into account a higher value of $\ell = 3$ mm, the deviation is around 8% and 12% for $\rho = 2$ mm and $\rho = 4$ mm, respectively.

Based on these analyses, it can be concluded that crack initiation can be successfully computed by considering the $\overline{\sigma}_{xx}(\ell)$ and $G_{inc}(\ell)$ functions derived from the circular submodel for crack initiation lengths of up to 0.3 mm and 0.2 mm for geometries with a central and eccentric hole, respectively.

5.2 Results discussion

Once the appropriate submodel size is determined, for each tested sample the average stress field and IERR functions are obtained through linear elastic FEA using plane strain elements. As presented in Sect. 2 and summarized in Table 1, 32 tested samples are analyzed featuring a central hole or an eccentric one with $e = 20$ mm. For each configuration, four hole radii $\rho = 0.5, 1, 2$ and 4 mm are considered. Boundary conditions are set by applying to the contour of the circular subdomain the displacements U_x and U_y measured by DIC, just before crack initiation. These displacements are depicted in Fig. 6 as a function of the curvilinear abscissae s, for a sample with $\rho = 4$ mm and $e = 0$ mm.

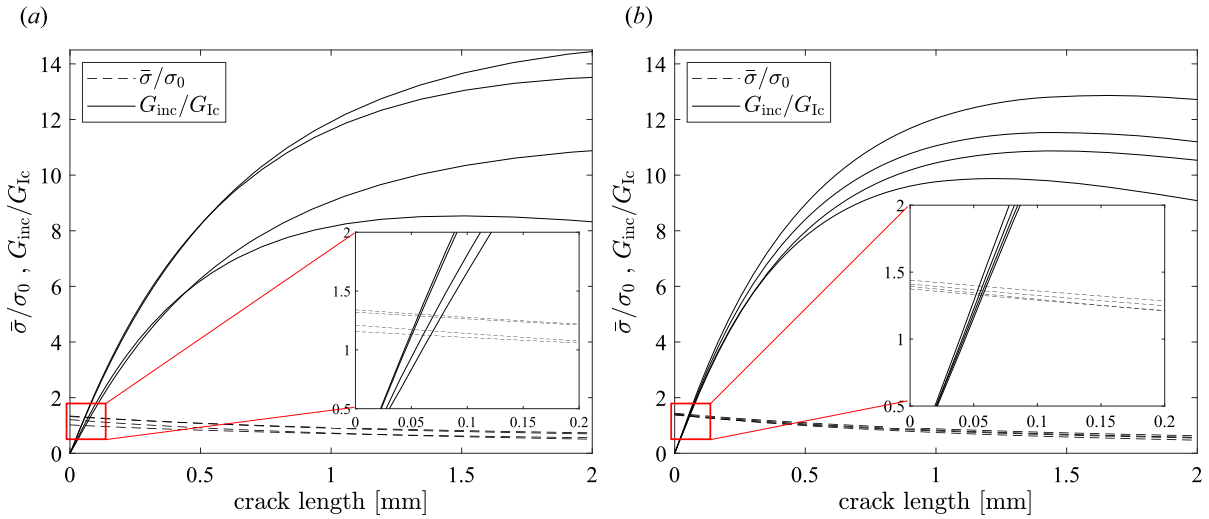

Fig. 9 Stress and energy conditions for the four samples with ρ = 4 mm, **a** e = 0 mm and **b** e = 20 mm

This approach enables the calculation of the average stress field $\overline{\sigma}_{xx}(\ell)$ and IERR $G_{inc}(\ell)$ functions corresponding to the initiation load U_c. Considering the FFM criterion expressed by Eq. (4), the three unknowns are: σ_0, G_{Ic} and ℓ_c.

Estimating the finite crack advance ℓ_c experimentally is not trivial since small length values are difficult to detect and measure accurately. Additionally, in most configurations, crack initiation is followed by unstable crack propagation, which further complicates the determination of ℓ_c. To investigate the initial crack initiation phase in more detail, Ferrian et al. (2024) employed an ultrahigh-speed acquisition camera with a sampling rate of 240,000 fps. However, even with this setup, it was not possible to accurately capture and measure the initiation length ℓ_c.

Regarding the determination of the critical energy release rate G_{Ic}, it can be obtained by analyzing the stable crack growth phase. Indeed, considering the LEFM condition for crack growth, $G(\ell_{exp})$ equals G_{Ic}, where ℓ_{exp} represents the experimental crack length. The value of $G(\ell_{exp})$ is computed using a circular 2D FE model concentric with the hole, through a J-integral calculation in Abaqus. The displacements measured by DIC for the experimental crack length ℓ_{exp}, are applied as boundary conditions to the FE model. With the experimental setup presented in Sect. 2, we are able to accurately monitor by DIC the crack length during the stable crack propagation phase for three samples with ρ = 2 mm and e = 20 mm (refer to Fig. 7). For the other specimens exhibiting stable crack growth, the crack tip can not be tracked due to the 1 fps acquisition rate and the small crack lengths involved. Thus, considering these three tested samples, a circular FE model with a crack of length ℓ_{exp} stemming from the hole with radius ρ = 2 mm is developed in Abaqus. The value of $G(\ell_{exp})$ is then computed from the J-integral using contour integrals.

Following this procedure, a value of G_{Ic} = 0.16 ± 0.03 MPa·mm is obtained.

Considering this value of the critical energy release rate, for each tested sample, the two unknowns of the FFM system σ_0 and ℓ_c are determined as the values satisfying Eq. (4), since $\ell_c < \ell^*$ for all the investigated configurations. Consequently, following this procedure for all the tested samples, σ_0 = 61 ± 17 MPa and ℓ_c = 0.09 ± 0.04 mm are determined.

It is worth noting that these values are influenced by the assumptions made during the analyses, particularly the submodeling hypothesis. In this study, we considered a 2D FE model with plane strain conditions, whereas slightly different results could be obtained if a 3D FE model was considered.

The value of the inherent material strength is close to the tensile strength determined by Ferrian et al. (2024) (σ_{UTS} = 67 ± 4.8 MPa), which was derived for the same material from the bending strength, experimentally measured through TPB tests. This finding also aligns with observations regarding brittle and quasi-brittle materials (Taylor 2004; Taylor et al.

2004, 2005). Regarding the critical crack advance ℓ_c, it keeps approximately constant as the hole eccentricity and radius vary, in agreement with the observations of Ferrian et al. (2024) and the results obtained by Sapora and Cornetti (2018) for a circular hole subjected to biaxial loading.

For the sake of completeness, after computing the average stress field $\overline{\sigma}_{xx}(\ell)$ and IERR $G_{inc}(\ell)$ functions corresponding to the initiation load $U_{c,}$ the pairs of values (σ_0, G_{Ic}) that satisfy Eq. (4) are depicted in Fig. 8a, b, for the tested samples with $\rho = 4$ mm, $e = 0$ mm and $\rho = 4$ mm, $e = 20$ mm, respectively. In both figures, red circles highlight the σ_0 values obtained by considering $G_{Ic} = 0.16$ MPa·mm.

Moreover, considering these tested samples, Fig. 8c, d report the corresponding critical crack advances ℓ_c for each (σ_0, G_{Ic}) pair solving Eq. (4). Taking into account $G_{Ic} = 0.16$ MPa·mm, for both configurations, the critical crack advance assumes small values ranging between 0.04 and 0.05 mm.

Finally, in Fig. 9a, b the stress and energy functions $\overline{\sigma}_{xx}/\sigma_0$ and G_{inc}/G_{Ic} are presented as the crack length ℓ varies, for the samples with $\rho = 4$ mm, $e = 0$ mm and $\rho = 4$ mm, $e = 20$ mm, respectively, considering $G_{Ic} = 0.16 \pm 0.03$ and $\sigma_0 = 61 \pm 17$ MPa. For these values of G_{Ic} and σ_0, the value of the intersection between the stress and energy conditions, ranges between 1.1 and 1.3 for the geometries with a central hole and between 1.3 and 1.4 for $e = 20$ mm.

6 Conclusions

In this study, we investigated the failure behavior of PMMA disks under uniaxial compression loading. Samples were characterized by the presence of either a central or eccentric circular hole.

A full finite element implementation of the Finite Fracture Mechanics (FFM) approach was presented, combining Digital Image Correlation (DIC) measurements with 2D linear elastic finite element analysis. Particularly, the displacements measured by DIC immediately before crack initiation were imposed to the contour of a circular FE model. This strategy provides a more realistic representation of the actual loading conditions compared to standard FFM implementations, which typically employ idealized prescribed forces or displacements. The critical energy release rate, G_{Ic}, was determined from the analysis of the stable crack growth phase using DIC-measured displacements. With this experimentally derived G_{Ic}, the method enables accurate estimation of the critical crack advance and the inherent material strength.

Building on these findings, future research could focus on refining the experimental setup to enable direct and accurate measurements of the critical crack advance, potentially by increasing acquisition rates, improving crack tip detection methods, or adopting alternative specimen geometries. Studies could also explore different materials and loading configurations to assess the generality of the approach. In addition, extending the methodology to 3D finite element models would allow an accurate representation of non-uniform crack fronts, enabling investigation of how variations in crack front shape influence the results.

Author contributions Francesco Ferrian: Conceptualization, Methodology, Experimental investigation, Data Curation, Numerical investigation, Writing—Original Draft, Realization of figures and plots. Alberto Sapora: Conceptualization, Methodology, Supervision of the Theoretical framework, Writing—Review and Editing, Supervision. Rafael Estevez: Conceptualization, Methodology, Supervision of the experimental campaign, Writing—Review and Editing, Supervision. Aurélien Doitrand: Conceptualization, Methodology, Supervision of the experimental campaign, Numerical investigations, Writing—Review and Editing, Supervision.

Funding Open access funding provided by Politecnico di Torino within the CRUI-CARE Agreement.

Data availability No datasets were generated or analysed during the current study.

Declarations

Conflict of interest The authors declare no conflict of interest.

Appendix: Determination of elastic properties through a DIC analysis

The elastic properties reported in Table 2 are determined by exploiting the DIC technique. The tensile and compressive moduli (E_t and E_c respectively) are compared for the PMMA tested by Ferrian et al. (2024). Regarding the tensile modulus E_t and Poisson's ratio υ, they were estimated following ASTM D638-14 (2014) standard code. Tensile tests were performed on plain specimens with dimensions of 70 mm length, 8 mm thickness, and 20 mm width. The strain fields, necessary to compute E_t and υ, are obtained by implementing DIC analysis and exploiting the strain gauge tool available in the software Ufreckles in a zone spanning over the specimen width.

Table 2 PMMA mechanical properties

E_t (GPa)	E_c (GPa)	υ
2.7 ± 0.03	2.7 ± 0.12	0.35 ± 0.014

The compressive modulus E_c is ultimately determined through a coupled approach, considering the displacement fields measured through DIC techniques and performing 2D linear elastic FEA. While in some studies, such as Molimard et al. (2005) and Lecompte et al. (2007), strain fields are measured to determine elastic properties, the present work directly compares the displacement fields instead. This approach aims to avoid amplifying measurement noise associated with numerical differentiation, as highlighted by Wang et al. (2011) and Azzouna et al. (2013).

Focusing on the configurations with a central hole presented in the previous section, the displacement fields U_x and U_y characterizing the sample surface under a specific applied load are determined using DIC for each sample. As presented in Sect. 3, the DIC measurements are performed using a camera with a resolution of 2392 (H) × 2774 (V) pixels and an acquisition rate of 1 fps. To achieve a good balance between surface partitioning and measurement noise, an unstructured mesh with 3-node triangular elements is applied using the software Ufreckles (Rethoré 2018), considering a mesh size of 60 pixels, equal to approximately 1.25 mm. The displacement values of the mesh nodes are evaluated within the ROI enclosed by the two concentric dashed circles depicted in

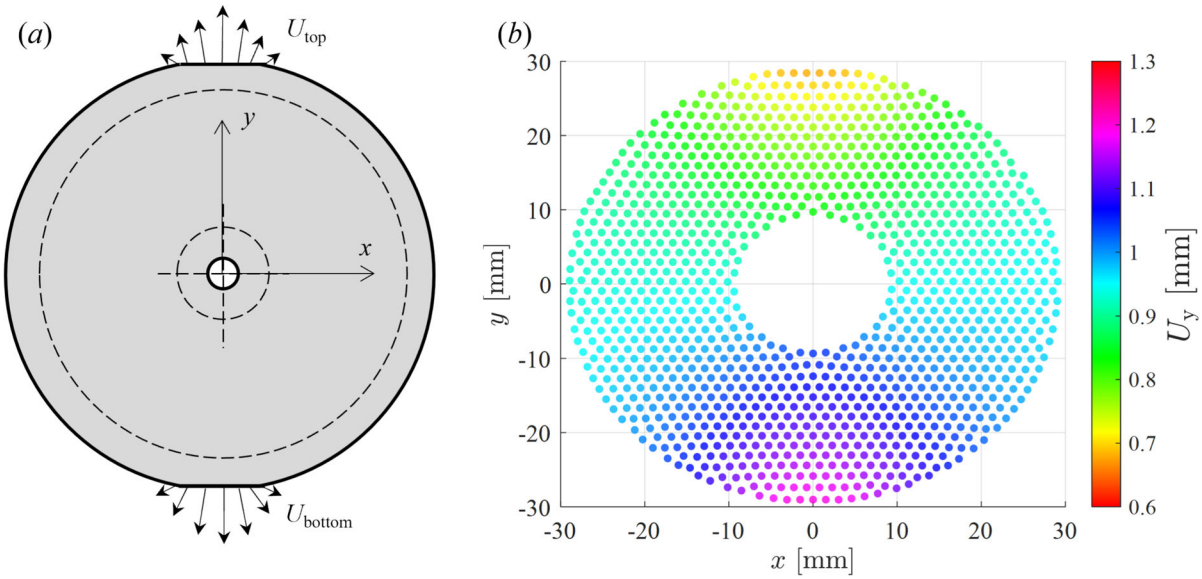

Fig. 10 **a** Detail of the investigated ROI enclosed by the two concentrical dashed circles and **b** displacement field U_y obtained by DIC for a sample with $e = 0$ mm and $\rho = 4$ mm. Please note that U_{top} and U_{bottom} denote the displacements close to the upper and lower contact zone, respectively

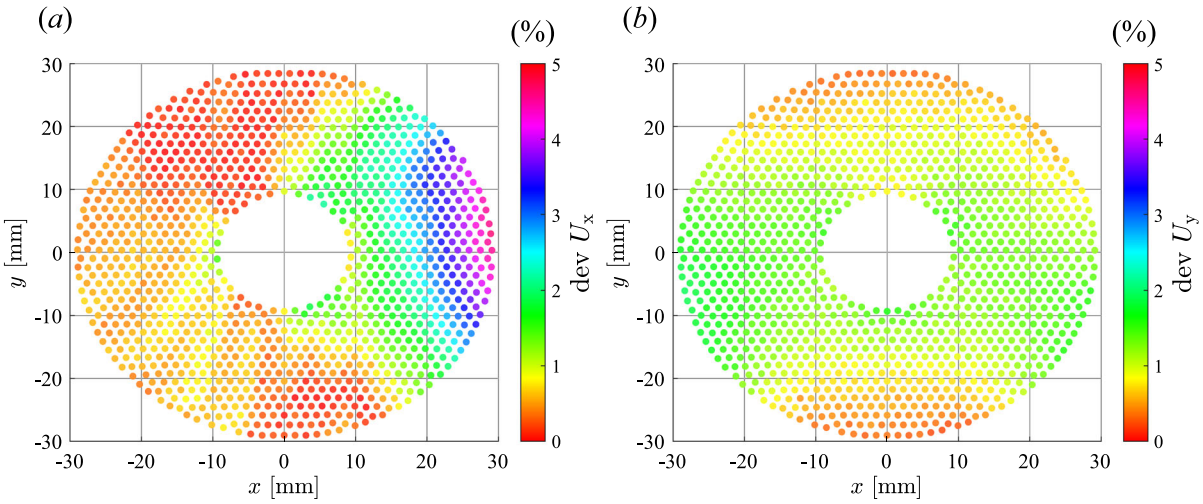

Fig. 11 Percentual deviations between displacement fields **a** U_x and **b** U_y obtained by DIC and FEA, for a sample with $e = 0$ mm and $\rho = 4$ mm

Fig. 10a. Furthermore, the displacements close to the two contact zones, denoted as U_{top} and U_{bottom}, are also obtained using DIC (Fig. 10a).

To assess the values of E_c and υ, for each tested sample presenting a central hole, 2D linear elastic FEA are performed by considering plane strain conditions and modeling the full geometry of the sample. A mesh with 4-node bilinear elements is adopted setting the minimum mesh size equal to 0.05 mm, following a convergence analysis. Boundary conditions are set by imposing U_{top} and U_{bottom} on the two flat ends. Subsequently, the displacement fields U_x and U_y are extracted from the same points evaluated by DIC. Finally, E_c and υ are determined by satisfying the following two requirements:

- the reaction force provided by FEA must equal the experimental one;
- the total deviation between the displacement fields determined by DIC and those obtained by FEA must be minimized. At each point, the percentage deviation is computed as $\mathrm{dev}U_i(x,y) = \left|U_i^{DIC}(x,y) - U_i^{FEA}(x,y)\right| / \left(\max\left(U_i^{DIC}\right) - \min\left(U_i^{DIC}\right)\right) \times 100$, where $(i = x, y)$, U_i^{DIC} and U_i^{FEA} are the displacement values determined through DIC and FEA, respectively.

This procedure is repeated for each of the 15 tested samples presenting a central hole. For the sake of clarity, the displacement field U_y obtained by DIC is depicted for only one tested sample with $e = 0$ mm and $\rho = 4$ mm, as shown in Fig. 10b. For this specimen, deviations between the displacement values obtained by DIC and FEA are lower than 5%, as illustrated in Fig. 11a, b.

The average values of the compressive modulus and Poisson's ratio estimated with this procedure are $E_c = 2.7 \pm 0.12$ GPa and $\upsilon = 0.36 \pm 0.02$, respectively. These are typical results for PPMA and closely align with those obtained from tensile tests on plain specimens (Ferrian et al. 2024), indicating the isotropic behavior of the tested PMMA and affirming the effectiveness of the proposed methodology.

References

(2014) ASTM D638-14, Standard test method for tensile properties of plastics. ASTM 1–15

(2022) Test methods for plane-strain fracture toughness and strain energy release rate of plastic materials

Aranda MT, Leguillon D (2023) Prediction of failure of hybrid composites with ultra-thin carbon/epoxy layers using the coupled criterion. Eng Fract Mech 281:109053. https://doi.org/10.1016/j.engfracmech.2023.109053

ASTM International (2018) ASTM D256-10 (2018). Standard test methods for determining the izod pendulum impact resistance of plastics, p 20

Awerbuch J, Madhukar MS (1985) Notched strength of composite laminates: predictions and experiments—a review. J Reinf Plast Compos 4:3–159. https://doi.org/10.1177/073168448500400102

Azzouna MB, Feissel P, Villon P (2013) Identification of elastic properties from full-field measurements: a numerical study of the effect of filtering on the identification results. Meas

Sci Technol 24:055603. https://doi.org/10.1088/0957-0233/24/5/055603
Chao Correas A, Sapora A, Reinoso J et al (2023) Coupled versus energetic nonlocal failure criteria: a case study on the crack onset from circular holes under biaxial loadings. Eur J Mech A/Solids 101:105037. https://doi.org/10.1016/j.euromechsol.2023.105037
Cornetti P, Pugno N, Carpinteri A, Taylor D (2006) Finite fracture mechanics: a coupled stress and energy failure criterion. Eng Fract Mech 73:2021–2033. https://doi.org/10.1016/j.engfracmech.2006.03.010
Doitrand A, Leguillon D, Estevez R (2020) Experimental determination of generalized stress intensity factors from full-field measurements. Eng Fract Mech 230:106980. https://doi.org/10.1016/j.engfracmech.2020.106980
Duminy T, Doitrand A, Meille S (2024) Fracture parameter identification by digital image correlation and finite fracture mechanics for millimeter-scale samples. Eng Fract Mech 295:109770. https://doi.org/10.1016/j.engfracmech.2023.109770
Felger J, Stein N, Becker W (2017) Mixed-mode fracture in open-hole composite plates of finite-width: an asymptotic coupled stress and energy approach. Int J Solids Struct 122–123:14–24. https://doi.org/10.1016/j.ijsolstr.2017.05.039
Ferrian F, Sapora A, Estevez R, Doitrand A (2024) Failure assessment of eccentric circular holes under compressive loading. Int J Fract. https://doi.org/10.1007/s10704-024-00805-3
Girard H, Doitrand A, Koohbor B et al (2023) Numerical simulation of fiber–matrix debonding: inverse identification of interface properties. Eng Fract Mech 286:109254. https://doi.org/10.1016/j.engfracmech.2023.109254
Girard H, Trand A, Koohbor B et al (2024) Comparison between 2D and 3D fiber-matrix debonding simulation for inverse identification of interface fracture properties. J Theor Comput Appl Mech. https://doi.org/10.46298/jtcam.12997
Hamam R, Hild F, Roux S (2007) Stress intensity factor gauging by digital image correlation: application in cyclic fatigue. Strain 43:181–192. https://doi.org/10.1111/j.1475-1305.2007.00345.x
Hild F, Roux S (2012) Digital image correlation. In: Optical methods for solid mechanics. A full-field approach, pp 183–228
Hild F, Bouterf A, Roux S (2015) Damage measurements via DIC. Int J Fract 191:77–105. https://doi.org/10.1007/s10704-015-0004-7
ISO (2023) ISO 180:2023 plastics, determination of izod impact strength, p 14
ISO13586 (2000) Plastics. Determination of fracture toughness (Gic and Kic). Linear elastic fracture mechanics (LEFM) approach. BSI London
Lecompte D, Smits A, Sol H et al (2007) Mixed numerical–experimental technique for orthotropic parameter identification using biaxial tensile tests on cruciform specimens. Int J Solids Struct 44:1643–1656. https://doi.org/10.1016/j.ijsolstr.2006.06.050
Leguillon D (2002) Strength or toughness? A criterion for crack onset at a notch. Eur J Mech A/Solids 21:61–72. https://doi.org/10.1016/S0997-7538(01)01184-6
Lin H, Xiong W, Yan Q (2016) Modified formula for the tensile strength as obtained by the flattened Brazilian disk test. Rock Mech Rock Eng 49:1579–1586. https://doi.org/10.1007/s00603-015-0785-z
Mantič V (2009) Interface crack onset at a circular cylindrical inclusion under a remote transverse tension. Application of a coupled stress and energy criterion. Int J Solids Struct 46:1287–1304. https://doi.org/10.1016/j.ijsolstr.2008.10.036
McNeill SR, Peters WH, Sutton MA (1987) Estimation of stress intensity factor by digital image correlation. Eng Fract Mech 28:101–112. https://doi.org/10.1016/0013-7944(87)90124-X
Molimard J, Le Riche R, Vautrin A, Lee JR (2005) Identification of the four orthotropic plate stiffnesses using a single open-hole tensile test. Exp Mech 45:404–411. https://doi.org/10.1007/BF02427987
Moore DR, Williams JG, Pavan A (2001) Fracture mechanics testing methods for polymers, adhesives and composites, 1st edn. Elsevier, London
Neuber H (1936) Theorie der technischen Formzahl. Forsch Ingenieurwes 7:271–274. https://doi.org/10.1007/BF02584908
Pan B (2011) Recent progress in digital image correlation. Exp Mech 51:1223–1235. https://doi.org/10.1007/s11340-010-9418-3
Pan B, Qian K, Xie H, Asundi A (2009) Two-dimensional digital image correlation for in-plane displacement and strain measurement: a review. Meas Sci Technol 20:062001. https://doi.org/10.1088/0957-0233/20/6/062001
Papšík R, Ševeček O, Schlacher J, Bermejo R (2024) Prediction of thermal shock induced cracking in multi-material ceramics using a stress-energy criterion. Eng Fract Mech 303:110121. https://doi.org/10.1016/j.engfracmech.2024.110121
Peters WH, Ranson WF (1982) Digital imaging techniques in experimental stress analysis. Opt Eng. https://doi.org/10.1117/12.7972925
Peterson RE (1938) Methods of correlating data from fatigue tests of stress concentration specimens. In: Macmillan (ed) Stephen Timoshenko anniversary volume, New York, p 179
Pipes RB, Wetherhold RC, Gillespie JW (1979) Notched strength of composite materials. J Compos Mater 13:148–160. https://doi.org/10.1177/002199837901300206
Réthoré J, Estevez R (2013) Identification of a cohesive zone model from digital images at the micron-scale. J Mech Phys Solids 61:1407–1420. https://doi.org/10.1016/j.jmps.2013.01.011
Réthoré J (2018) UFreckles. https://doi.org/10.5281/ZENODO.1433776
Rheinschmidt F, Drass M, Schneider J, Rosendahl PL (2024) Cavitation and crack nucleation in thin hyperelastic adhesives. Int J Fract 247:33–49. https://doi.org/10.1007/s10704-024-00776-5
Roux S, Hild F (2006) Stress intensity factor measurements from digital image correlation: post-processing and integrated approaches. Int J Fract 140:141–157. https://doi.org/10.1007/s10704-006-6631-2

Sakha M, Nejati M, Driesner T (2023) On the initiation of hydraulic fractures in anisotropic rocks. Int J Rock Mech Min Sci 169:105429. https://doi.org/10.1016/j.ijrmms.2023.105429

Sapora A, Cornetti P (2018) Crack onset and propagation stability from a circular hole under biaxial loading. Int J Fract 214:97–104. https://doi.org/10.1007/s10704-018-0315-6

Sapora A, Torabi AR, Etesam S, Cornetti P (2018) Finite fracture mechanics crack initiation from a circular hole. Fatigue Fract Eng Mater Struct 41:1627–1636. https://doi.org/10.1111/ffe.12801

Schindler H-J (2018) Fracture toughness for engineering application: there is a need for more suitable testing standards. Procedia Struct Integr 13:398–403. https://doi.org/10.1016/j.prostr.2018.12.066

Seweryn A (1994) Brittle fracture criterion for structures with sharp notches. Eng Fract Mech 47:673–681. https://doi.org/10.1016/0013-7944(94)90158-9

Shen B, Paulino GH (2011) Direct extraction of cohesive fracture properties from digital image correlation: a hybrid inverse technique. Exp Mech 51:143–163. https://doi.org/10.1007/s11340-010-9342-6

Susmel L, Taylor D (2008) On the use of the theory of critical distances to predict static failures in ductile metallic materials containing different geometrical features. Eng Fract Mech 75:4410–4421. https://doi.org/10.1016/j.engfracmech.2008.04.018

Sutton M, Wolters W, Peters W et al (1983) Determination of displacements using an improved digital correlation method. Image vis Comput 1:133–139. https://doi.org/10.1016/0262-8856(83)90064-1

Tan SC (1987) Fracture strength of composite laminates with an elliptical opening. Compos Sci Technol 29:133–152. https://doi.org/10.1016/0266-3538(87)90053-4

Tanaka K (1983) Engineering formulae for fatigue strength reduction due to crack-like notches. Int J Fract 22:R39–R46. https://doi.org/10.1007/BF00942722

Taylor D (2004) Predicting the fracture strength of ceramic materials using the theory of critical distances. Eng Fract Mech 71:2407–2416. https://doi.org/10.1016/j.engfracmech.2004.01.002

Taylor D (2007) The theory of critical distances. Elsevier, London

Taylor D, Merlo M, Pegley R, Cavatorta MP (2004) The effect of stress concentrations on the fracture strength of polymethylmethacrylate. Mater Sci Eng A 382:288–294. https://doi.org/10.1016/j.msea.2004.05.012

Taylor D, Cornetti P, Pugno N (2005) The fracture mechanics of finite crack extension. Eng Fract Mech 72:1021–1038. https://doi.org/10.1016/j.engfracmech.2004.07.001

Torabi AR, Etesam S, Sapora A, Cornetti P (2017) Size effects on brittle fracture of Brazilian disk samples containing a circular hole. Eng Fract Mech 186:496–503. https://doi.org/10.1016/j.engfracmech.2017.11.008

Vereecke J, Bois C, Wahl J-C et al (2024) Explicit modelling of meso-scale damage in laminated composites—comparison between finite fracture mechanics and cohesive zone model. Compos Sci Technol 253:110640. https://doi.org/10.1016/j.compscitech.2024.110640

Wang Q-Z, Xing L (1999) Determination of fracture toughness KIC by using the flattened Brazilian disk specimen for rocks. Eng Fract Mech 64:193–201. https://doi.org/10.1016/S0013-7944(99)00065-X

Wang Q, Jia X, Kou S et al (2004) The flattened Brazilian disc specimen used for testing elastic modulus, tensile strength and fracture toughness of brittle rocks: analytical and numerical results. Int J Rock Mech Min Sci 41:245–253. https://doi.org/10.1016/S1365-1609(03)00093-5

Wang W, Mottershead JE, Sebastian CM, Patterson EA (2011) Shape features and finite element model updating from full-field strain data. Int J Solids Struct 48:1644–1657. https://doi.org/10.1016/j.ijsolstr.2011.02.010

Weißgraeber P, Hell S, Becker W (2016a) Crack nucleation in negative geometries. Eng Fract Mech 168:93–104. https://doi.org/10.1016/j.engfracmech.2016.02.045

Weißgraeber P, Leguillon D, Becker W (2016b) A review of finite fracture mechanics: crack initiation at singular and non-singular stress raisers. Arch Appl Mech 86:375–401. https://doi.org/10.1007/s00419-015-1091-7

Whitney JM, Nuismer RJ (1974) Stress fracture criteria for laminated composites containing stress concentrations. J Compos Mater 8:253–265. https://doi.org/10.1177/002199837400800303

Wu S, Ma J, Cheng Y et al (2018) Numerical analysis of the flattened Brazilian test: failure process, recommended geometric parameters and loading conditions. Eng Fract Mech 204:288–305. https://doi.org/10.1016/j.engfracmech.2018.09.024

Yan Z, Dai F, Liu Y et al (2021) New insights into the fracture mechanism of flattened Brazilian disc specimen using digital image correlation. Eng Fract Mech 252:107810. https://doi.org/10.1016/j.engfracmech.2021.107810

Yue Z, Peng L, Qiao Y et al (2022) Dynamic brittle fracture in sharp V-notched rock specimens using digital image correlation method. Theor Appl Fract Mech 119:103323. https://doi.org/10.1016/j.tafmec.2022.103323